Chemical Science

ROYAL SOCIETY OF CHEMISTRY

EDGE ARTICLE

View Article Online
View Journal

Cite this: DOI: 10.1039/d6sc03073d

All publication charges for this article have been paid for by the Royal Society of Chemistry

Received 14th April 2026
Accepted 5th June 2026

DOI: 10.1039/d6sc03073d

rsc.li/chemical-science

Chalcogen-bonding-mediated chiral recognition and enantioenrichment of organoselenocyanates

Tianhao Wang, Aiyou Hao * and Pengyao Xing *

Chalcogen bonding (ChB) is recognized as an essential intermolecular interaction in Group VIA element-containing materials. The multiple σ-holes with high directionality endow ChB with potential for chiral functions, including recognition, sensing and chiroptical materials. Herein, we employ ChB to enable chiral sensing and enantioenrichment and separation of organoselenocyanates. A library of organic selenocyanate derivatives was constructed, and their complexation with a chiral phenanthroline conjugated foldamer was driven by ChB, aided by hydrogen bonding and π-stacking forces. The deep chiral environment of the foldamer enables binding affinity bias towards enantiopure selenocyanates, yielding differential spectroscopic output and binding constants. ChB-mediated chiral recognition also impacts self-assembly, indicating that the emergence of macroscopic chirality is controlled by the enantiomeric matching effect. Finally, we realized efficient enantioenrichment of the organoselenocyanates utilizing ChB-assisted chiral recognition for the first time, which establishes a new route for the chiral separation of Se-containing pharmaceuticals by σ-hole interactions.

Introduction

Chiral recognition is fundamentally important in chemistry, pharmaceuticals, and materials science, with significant implications in the synthesis and purification of chiral drugs, asymmetric catalysis, and supramolecular chemistry.[1–10] Its selectivity benefits from the directionality and synergistic effects of multiple weak forces, while its dynamic nature results in reversibility, enabling excellent adaptivity and tunability. These advantages have promoted the widespread applications of chiral recognition based on noncovalent interactions, such as van der Waals forces, electrostatic interactions, hydrogen bonding (HB), and π–π stacking, across various fields, including drug molecule recognition, the design of chiral sensors, chiral separation media, molecular machines, and catalysis.[11–15] ChB commonly occurs in the form of EWG-Ch⋯LB, where EWG refers to an electron-withdrawing group, LB is a Lewis base, and Ch represents a chalcogen element (O, S, Se and Te).[16,17] The noncovalent interactions between the electropositive σ-hole and the electronegative region of the Lewis base constitute the ChB. Although ChB has been known for several decades, its application remains largely underexplored and insufficiently utilized. Current research on ChB is mainly focused on areas such as anion transport,[18–22] catalysis[23–27] and crystal engineering.[28–33] In contrast, studies involving its use in chiral recognition and separation are still very limited.[34,35]

Organoselenocyanate compounds have demonstrated promising anticancer activity and have been extensively studied as potential anticancer agents[36–39] (Scheme 1a). Meanwhile, organoselenocyanates, as an important class of selenium-containing compounds, exhibit potential as ChB donors. The strong electron-withdrawing ability of –CN induces a deep σ-hole on Se. The key interactions through which these compounds recognize and bind to biological receptors to exert their pharmacological effects mainly include ChB, HB, and π–π interactions (Scheme 1a).[39] Exploring the role of ChB in supramolecular complexation will deepen the understanding of drug metabolism and facilitate the enantiomeric sensing and enrichment of organoselenocyanates, which has not been achieved previously.

Here, we aim to mimic the recognition of organoselenocyanate-based anticancer agents by a chiral foldamer (Scheme 1b). The host Pyr comprises pyrenes and phenanthroline conjugated with a chiral binaphthyl skeleton, which forms a deep chiral environment as a result of intramolecular folding. The efficient recognition of selenocyanates (Chart 1) is enabled by the ChB, aided by the HB and π-stacking forces. The synergistic effects enable efficient chiral sensing with distinct spectroscopic output bias (Scheme 1c). The chiral matching effects also affect the expression of macroscopic chirality, whereby the nanotopology of self-assemblies could be controlled. We also realized efficient enantioenrichment and separation of selenocyanates by co-assembly with the foldamer. The successful application of ChB in chiral recognition and resolution expands the scope of ChB utilization and offers a new perspective for chiral recognition and separation.

School of Chemistry and Chemical Engineering, Shandong University, Jinan, Shandong, 250100, P. R. China. E-mail: haoay@sdu.edu.cn; xingpengyao@sdu.edu.cn

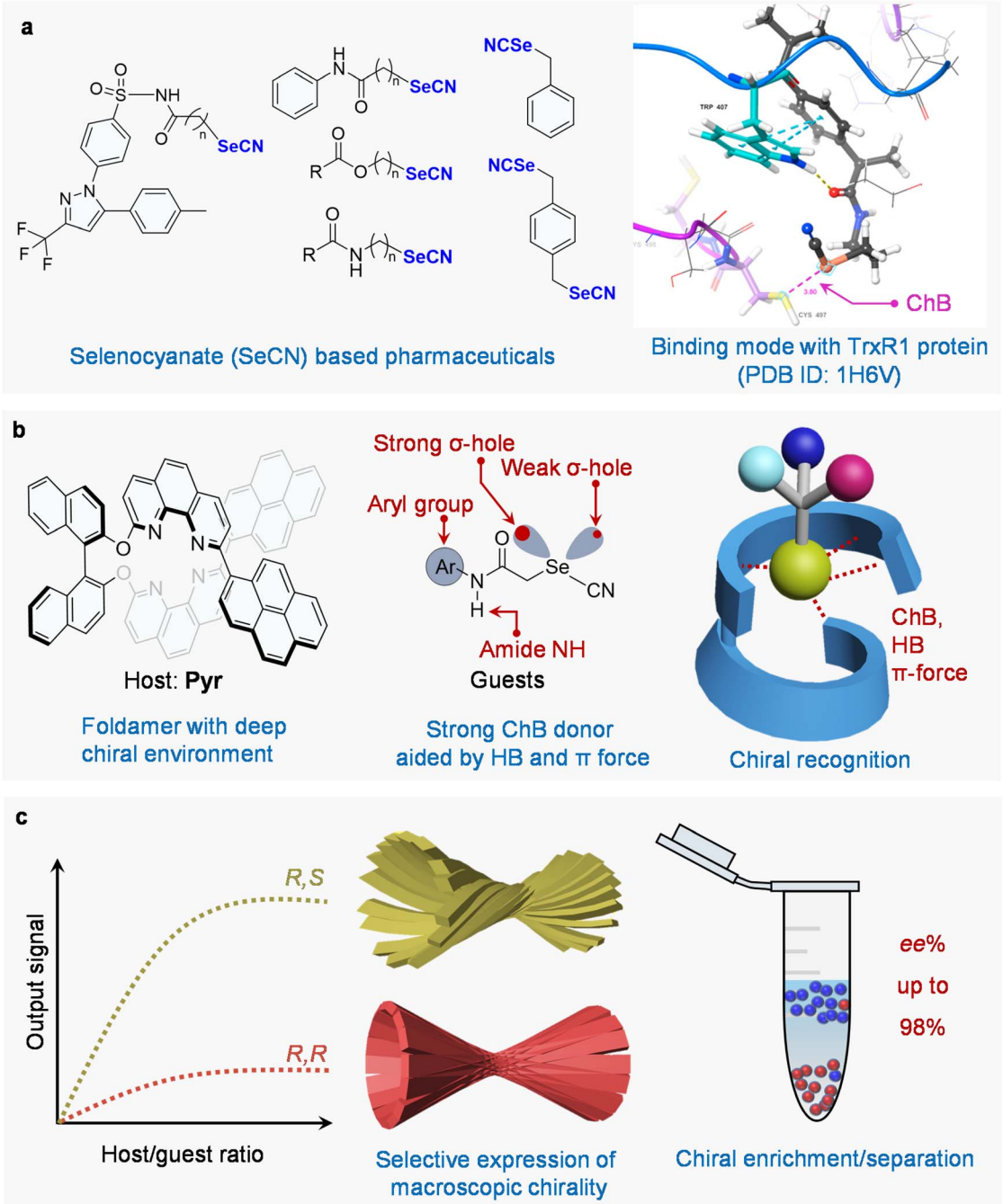

Scheme 1 (a) Several common selenocyanate (SeCN) anticancer drugs and their binding patterns with TrxR1 protein (PDB ID: 1H6V), adapted with permission from ref. 39. (b) Folding host molecule Pyr with a deep chiral environment, and the design of guest molecules with strong ChB donors; chiral recognition mode between host and guest through ChB, HB and π-forces. (c) Chiral recognition between the host and guest molecules exhibiting different morphologies and achieving chiral separation with high ee% values.

Results and discussion

Synthesis and structure

The host Pyr was synthesized through aromatic nucleophilic substitution followed by a Suzuki–Miyaura coupling reaction. For the selenocyanates, the amide intermediates (α-Cl amides) were obtained *via* amidation reaction between a chiral amine and chloroacetyl chloride. Then, the guest molecules were synthesized through a nucleophilic substitution reaction with KSeCN. More detailed experimental procedures are provided in the SI. The successful synthesis was confirmed through nuclear magnetic resonance (^{1}H, ^{13}C and ^{77}Se NMR) and mass spectrometry (details can be found in the SI). Single crystals of the guest molecules MBA and DHIA, as well as of the host molecule, were successfully obtained *via* the solvent evaporation method (Fig. 1a–d). Two crystal forms of MBA were obtained by

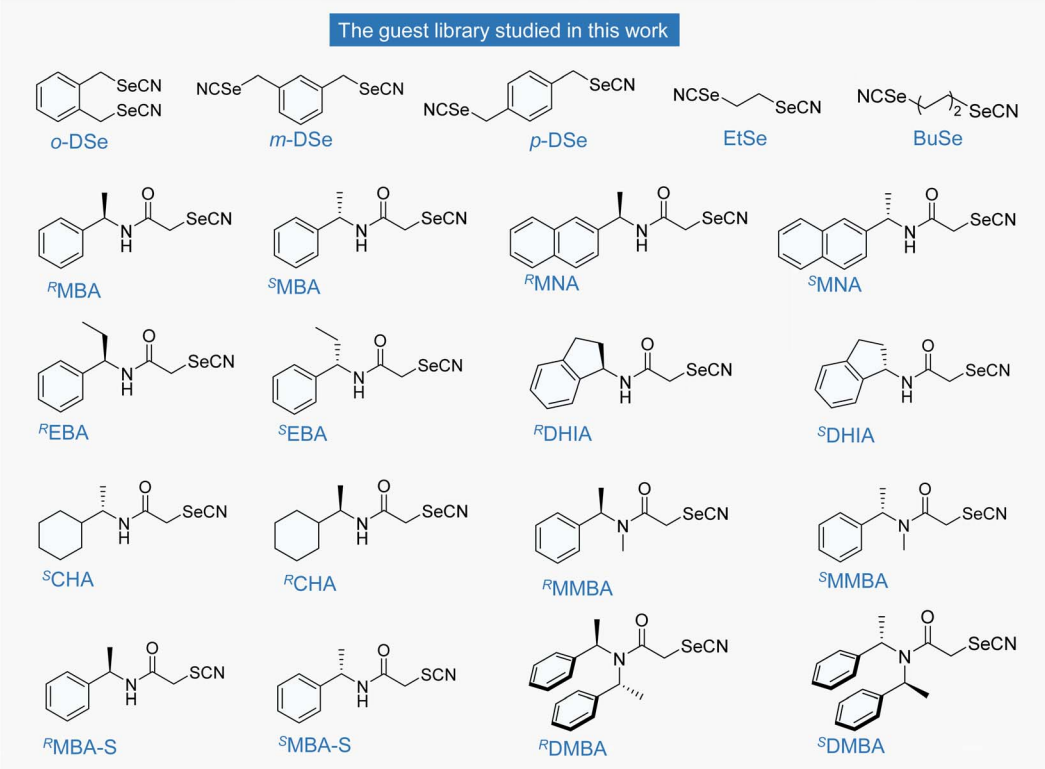

Chart 1 The guest library studied in this work.

adjusting the solvent conditions. ChB was observed in the crystal structures, including both intramolecular and intermolecular forms. In α-MBA, intermolecular interactions are formed between the lone pair electrons of the carbonyl group and the strong σ-hole site on Se (2.824 Å, ∠C–Se–O = 168.5°). In β-MBA, the interaction occurs in a linear form between the lone pair electrons on the N of the cyano group and the strong σ-hole on Se (3.077 Å, ∠C–Se–N = 173.3°). The two forms are respectively crystallized in $CHCl_3$/MeOH and CH_2Cl_2/MeOH, and the adaptive feature verifies the great potential of SeCN in ChB formation. In DHIA, two types of ChB are present: one involves an intramolecular interaction between the carbonyl group and a σ-hole on Se (2.891 Å, ∠C–Se–O = 149.0°), while the other involves an intermolecular interaction involving the π-electrons of the cyano group and a weaker σ-hole on Se (3.494 Å, ∠C–Se–π = 153.8°). It should be noted that the d_{Se-N} of 3.376 Å is within the sum of the van der Waals radii of Se and N (345 pm), yet the lone pair electrons of the cyano N are located perpendicular to –C≡N. Thus, the Se–N ChB is excluded due to the false angle. The crystal structure of the host Pyr reveals a folded conformation. The two phenanthroline units connected *via* a binaphthyl linker exhibit π–π stacking arrays, while the two pyrene rings attached to the pyrroline units are locked through CH–π interactions, exhibiting an overall folding conformation. The molecular electrostatic potential (MESP) was calculated using the Gaussian 16 program at the DFT(B3LYP)/6-311G(d,p) level of theory (Fig. 1e and S1).[40] The electron-rich region of Pyr exhibits a negative potential as low as −42.2 kcal mol^{-1}, while MBA features a strong σ-hole with $V_{S,max}$ = 41.8 kcal mol^{-1} (σ* of Se–CN bond) and a weaker σ-hole measuring $V_{S,max}$ = 23.8 kcal mol^{-1} (σ* of Se–CH_2 bond). Compared to typical benzoselenadiazole derivatives, which typically exhibit a $V_{S,max}$ ≈ 20–30 kcal mol^{-1} on Se, these selenocyanate compounds demonstrate significantly enhanced σ-hole potential.[41,42] It exhibits biaxial σ-holes thanks to the presence of CN and carbonyl group at the α-position, which enables enhanced ChB with the hosts.

Interaction between host and guest

The complexation between Pyr and selenocyanate was investigated under solution conditions. Unless otherwise specified, all solution-phase experiments described below were carried out in a chloroform/methylcyclohexane mixture with a volume ratio of 1 : 39, at a host concentration of 0.05 mM. A titration experiment was conducted with the guest by preparing a series of solutions in which the host concentration was fixed at 0.05 mM while the guest concentration was gradually increased. UV-vis absorption and fluorescence titration experiments were performed in $CHCl_3$/methylcyclohexane (MCH) (Fig. 2a and b). Upon host–guest complexation, the local electronic environment of the chromophoric units is perturbed by specific noncovalent interactions. This perturbation enhances the effective electronic transition probability, leading to an increase in molar absorptivity. Moreover, upon gradual addition of the guest, host–guest complex formation enhances the overall aggregation of the system, leading to a corresponding increase in the

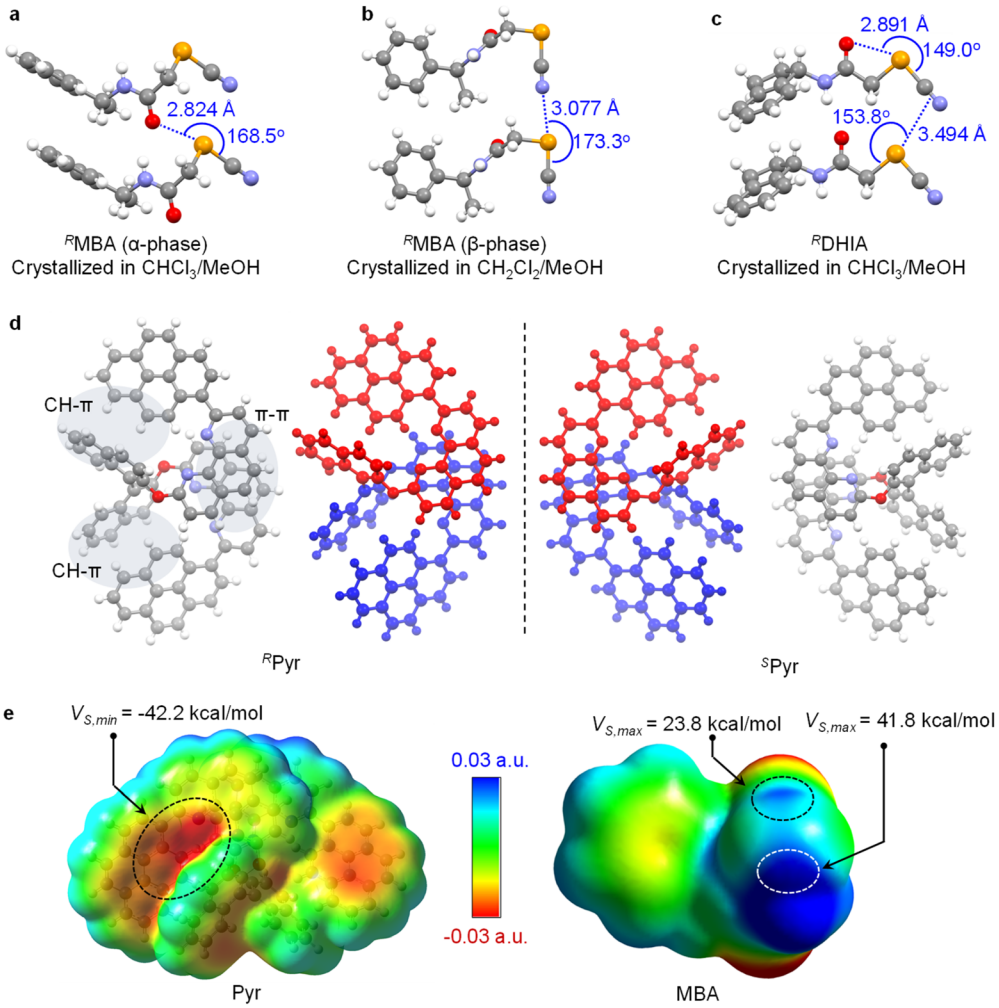

Fig. 1 (a–c) X-ray structures of α-^{R}MBA, β-^{R}MBA, and ^{R}DHIA (CCDC No: 2469791, 2469788 and 2469789). (d) X-ray structures of Pyr (CCDC No.: 2469790). (e) Electrostatic potential maps of the Pyr and MBA.

absorption baseline. Meanwhile, complex formation opens additional nonradiative relaxation pathways in the excited state, resulting in fluorescence quenching. Based on the spectroscopic variations, binding affinities could be clearly determined. In benzyl diselenocyanates and their analogues, including *o*-DSe, *m*-DSe and *p*-DSe (Fig. 2c and d), only *o*-DSe exhibited binding activity, while *m*-DSe and *p*-DSe remained inactive. This behavior may be attributed to the shorter distance between the two SeCN groups in *o*-DSe, which synergistically enhanced the complexation with phenanthroline groups. Aliphatic selenocyanates BuSe and EtSe with distinct alkyl spacers were further investigated, but they showed inactive binding with Pyr. These selenocyanates or their analogues indiscriminately show Se–N ChB in solid state X-ray structures,[43–46] while in the present diluted (0.05 mM) state, they exhibit significant selectivity based on spectral changes. Subsequently, guest molecules containing aryl and amide units—MBA, EBA, DHIA, and MNA—were investigated. Based on changes in the absorption and fluorescence intensities at 430 nm, all four guests exhibited active binding affinity with Pyr (Fig. 2c and d). To evaluate the contributions of the three types of interactions, a series of MBA derivatives were designed as control compounds: (1) replacing the phenyl ring with a cyclohexyl group to give CHA, thereby eliminating π–π interactions; (2) substituting the –SeCN with the weaker σ-hole donor –SCN to obtain MBA–S, in order to isolate the effect of ChB; and (3) functionalizing the N–H to generate MMBA and DMBA, to assess the necessity of HB. Remarkably, all four control compounds exhibited inactive binding with Pyr, indicating that π–π interactions, HB, and ChB are all essential for recognition and binding. ChB serves as the primary directional driving force in the recognition process. The strongly electron-withdrawing –CN substituent induces a pronounced σ-hole on the Se center, enabling the formation of highly linear and directional ChB interactions with the electron-rich sites of Pyr, thereby anchoring the guest within the chiral cavity. HB further stabilizes the host–guest complex by locking the guest conformation. Specifically, the amide N–H moieties establish hydrogen bonds with the heteroatom sites of Pyr, fixing the guest orientation and promoting stereospecific complementarity within the chiral

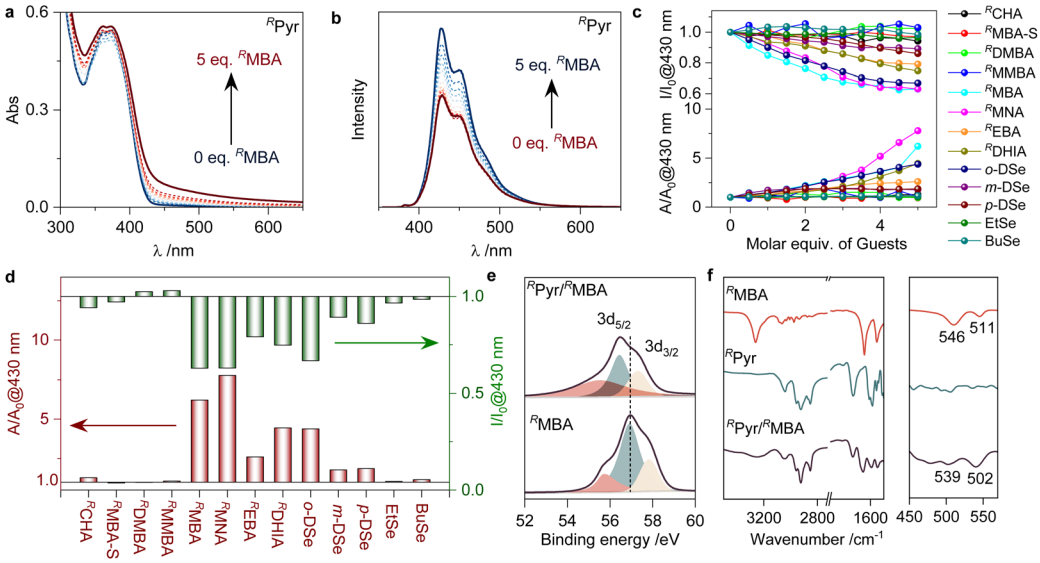

Fig. 2 (a) UV-vis titration spectra for ^{R}MBA with ^{R}Pyr (0.05 mM, $CHCl_3$/methylcyclohexane (MCH), v/v = 1 : 39). (b) Fluorescence titration spectra for ^{R}MBA with ^{R}Pyr (0.05 mM, $CHCl_3$/MCH, v/v = 1 : 39). (c) Absorbance enhancement ratio (A/A_0) at 430 nm and the fluorescence quenching ratio (I/I_0) at 430 nm as a function of guest equivalents. (d) Histogram of absorbance enhancement ratio (A/A_0) at 430 nm and the fluorescence quenching ratio (I/I_0) at 430 nm. (e) XPS spectra of ^{R}MBA before and after interaction with ^{R}Pyr. The powders used were collected self-assemblies (Pyr/guest 1 : 1, 0.125 mM, $CHCl_3$/MCH, v/v = 1 : 39). (f) Infrared (IR) spectra of self-assembled ^{R}MBA, ^{R}Pyr, and their complex. The powders used were collected self-assemblies (Pyr/guest 1 : 1, 0.125 mM, $CHCl_3$/MCH, v/v = 1 : 39).

environment. In addition, π–π stacking interactions expand the intermolecular contact interface and enhance chiral discrimination through aromatic matching between the host and guest frameworks, ultimately contributing to increased binding affinity and enantioselectivity. The absence of any one of these interactions leads to a loss of binding activity. These findings confirm that the host is capable of specifically recognizing and binding organoselenocyanates, demonstrating its high selectivity and molecular recognition capability.

To obtain the assembled state in this solvent system, the solution concentration was increased to 0.125 mM. All subsequent assembly experiments were conducted under the same conditions. Solid powders were obtained by centrifugation under the assembly conditions, followed by X-ray photoelectron spectroscopy (XPS) analysis (Fig. 2e). In the binding energies of the Se $3d_{5/2}$ and $3d_{3/2}$ orbitals, a decreasing trend was observed after introducing Pyr, providing further evidence for the formation of ChB. This may be attributed to an increase in the electron cloud density around the Se upon ChB formation. In addition, the σ-hole is partially filled, resulting in a more uniform electron distribution. These changes enhance the shielding effect, thereby reducing the binding strength of the 3d electrons, which is manifested in XPS as a left shift and a decrease in binding energy. Meanwhile, the assembled-state solids prepared under identical conditions were analyzed by infrared spectroscopy using the KBr pellet method (Fig. 2f). The N–H vibration band of the amide group appeared at 3262 cm^{-1}, and upon interaction with Pyr, this band showed significant broadening, indicating the formation of hydrogen bonding. Correspondingly, the C=O stretching vibration also exhibits noticeable changes after complexation. This can be attributed to the disruption of intramolecular hydrogen bonding and ChB involving the carbonyl oxygen in MBA. Additionally, the Se–C vibrations were observed at 546 and 511 cm^{-1}, corresponding to the Se–CN and Se–CH_2 bonds, respectively. After interaction with Pyr, both bands are red-shifted, suggesting the weakening and lengthening of the Se–C bonds. This observation is consistent with the formation of ChB.

Then, a series of samples was prepared in $CDCl_3$ for NMR analysis. To facilitate investigation of the NMR spectral changes of the guest, the guest concentration was fixed at 1 mM while the host concentration was gradually increased, and NMR titration experiments were then performed (Fig. 3a and b). A pronounced downfield shift was observed for H_a, indicating the formation of a hydrogen bond. H_c, located at the α-position of the carbonyl group, exhibits a downfield shift due to its proximity to the deshielding region of the aromatic ring. This shift is attributed to the ChB interaction between the SeCN group and Pyr, which brings H_c closer to the aromatic system. In contrast, the benzylic proton H_b showed an upfield shift due to the π–π stacking, which typically requires a parallel arrangement of aromatic rings, while H_b lies perpendicular to the aromatic plane, placing it within the shielding region of the aromatic system. Furthermore, two-dimensional ^{1}H–^{1}H nuclear Overhauser effect spectroscopy (NOESY) experiments were performed under the same conditions as those used for the NMR titration studies. It confirmed a strong spatial interaction between the aromatic protons of MBA and the protons on the phenanthroline, providing evidence for the presence of π–π interactions with MBA (Fig. 3c). The Pyr–MBA complex model was calculated using the Gaussian 16 program at the DFT (B3LYP)/6-311G(d,p) level of theory with the inclusion of D3

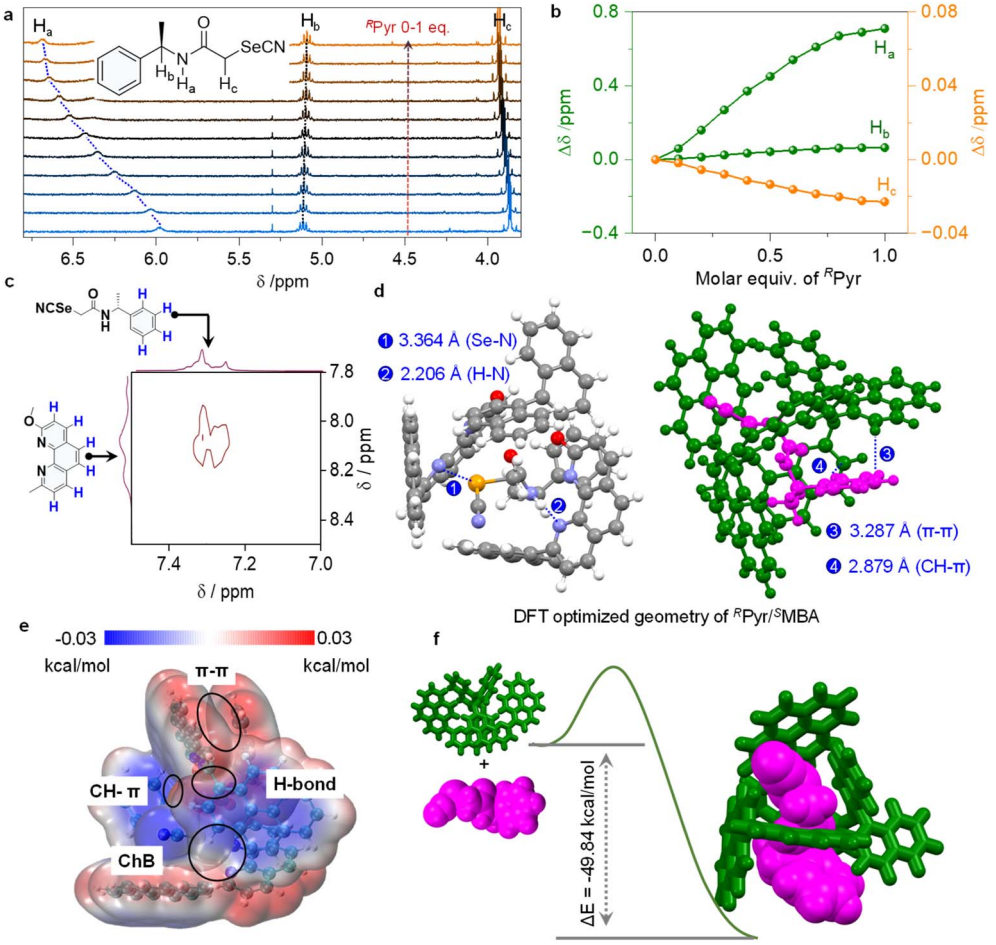

Fig. 3 (a) ^{1}H NMR titration spectra for ^{R}MBA (1 mM in $CDCl_3$) with increasing ^{R}Pyr from 0 to 1 equiv. (b) Plots of chemical shift changes for individual protons of the ^{1}H NMR titration as a function of added Pyr equivalents. (c) 2D-NOESY spectrum for ^{R}MBA/^{R}Pyr mixture (1 mM, 1 : 1, in $CDCl_3$). (d) Optimized binding mode between ^{S}MBA and ^{R}Pyr calculated at the B3LYP/6-311G (d,p) theory level; some of the hydrogens were omitted for clarity. (e) Taking ^{R}Pyr and ^{S}MBA as an example, intermolecular interactions were analyzed using a penetration map between molecules. (f) Schematic diagram of the binding energy of ^{R}Pyr and ^{S}MBA.

dispersion correction, and the binding was evaluated with correction for basis set superposition error (Fig. 3d). The phenanthroline–pyrene conjugate has an overall electron-rich region whereby Se (σ-hole at the σ* of Se–CN bond) forms multiple bonds with both N atoms and π planes. Synergistically, N–H and phenyl groups are involved in the HB and π-stacking arrangements, which agrees with the structure–property correlations as discussed above. Subsequently, the MESP between the host and the guest was analyzed under the same basis set (Fig. 3e). The existence of ChB, HB and π-stacking interactions can be clearly observed. The binding energy between the host and the guest was also calculated (Fig. 3f and S2), and the binding energy between ^{R}MBA and ^{R}Pyr was approximately −49.8 kcal mol^{-1}.

Evaluation of chirality recognition

Samples were prepared following the same procedure, and ^{77}Se NMR spectroscopy was subsequently performed. In the ^{77}Se NMR spectra (Fig. 4a), upon interaction with ^{S}Pyr, the selenium signals of the MBA enantiomers shifted upfield towards different positions. It seems that ^{R}MBA exhibited a stronger binding affinity toward ^{S}Pyr compared to ^{S}MBA. These observations provide further evidence for the presence of ChB, also indicating a chiral recognition and matching effect. Then, UV-vis absorption and fluorescence titration experiments were further conducted on different enantiomers (Fig. 4b and S16–S23). A clear difference in the absorption variations (A/A_0) between ^{R}Pyr and MBA enantiomers was observed. Consistent with the ^{77}Se NMR results, ^{R}Pyr exhibited stronger binding affinity toward ^{S}MBA, ^{R}MNA, ^{R}EBA and ^{R}DHIA, which may result from a mismatch between the spatial specificity required by Pyr and the conventional stereochemical naming rules. Nevertheless, this discrepancy does not affect the validity of the subsequent investigations. The absorption enhancement ratios of all chiral guests after interaction with ^{R}Pyr are quantified and summarized in Fig. 4c. To evaluate the chiral recognition capability of Pyr for each guest, the ratio of absorption enhancement between the two enantiomers of the same guest was calculated (Fig. 4g). The resulting order of chiral recognition was: MNA > DHIA > MBA > EBA.

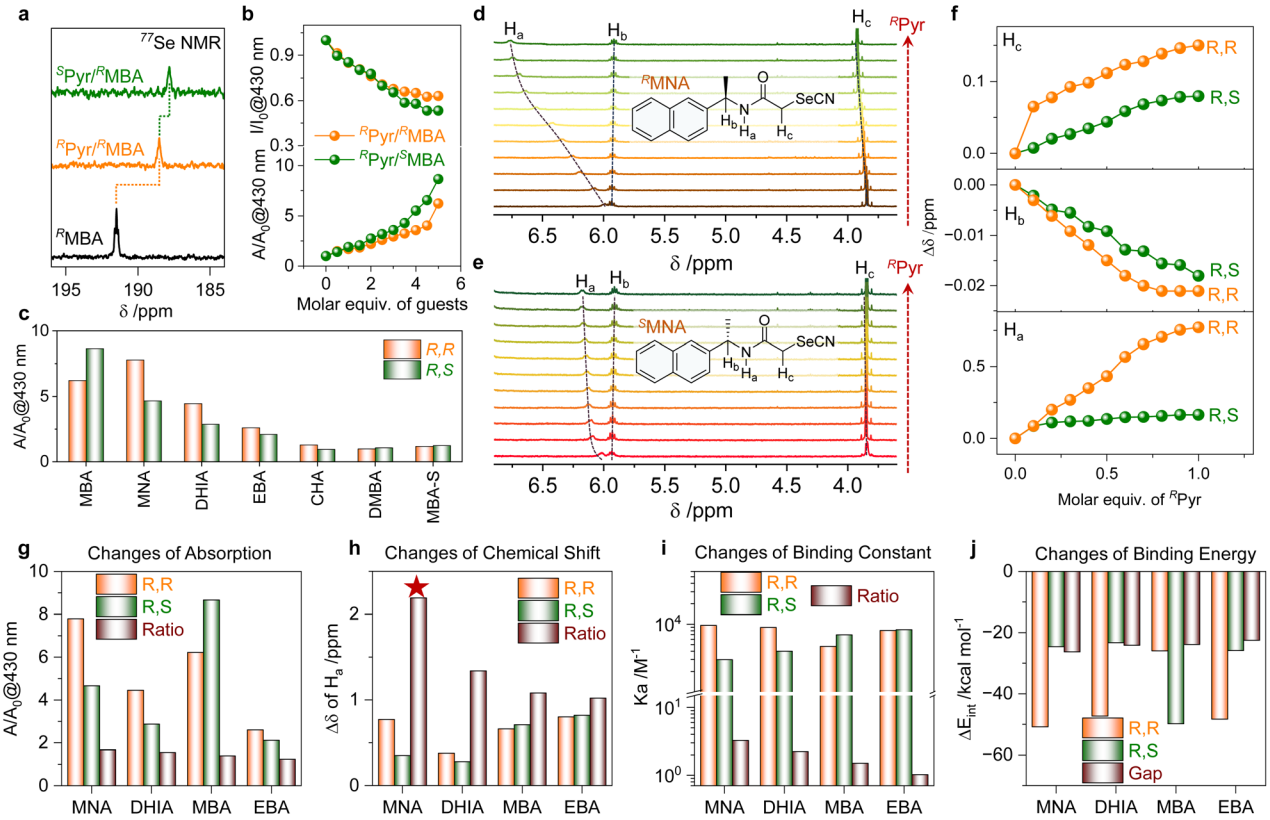

Fig. 4 Enantiomeric selectivity. (a) ^{77}Se NMR spectra for MBA before and after interaction with Pyr (1 mM in $CDCl_3$). (b) A/A_0 and I/I_0 as a function of guest concentration. (c) Absorption enhancement for each guest. (d and e) ^{1}H NMR titration spectra for ^{R}MNA and ^{S}MNA (0.01 mM in $CDCl_3$) with ^{R}Pyr increasing from 0 to 1 equiv. (f) Plot of chemical shift changes for individual protons during the NMR titration experiment as a function of Pyr equivalents. Chiral recognition ability recorded *via* several parameters, including changes of (g) absorption, (h) chemical shift, (i) binding constant (K_a) and (j) binding energies calculated at the B3LYP/6-311(d,p) level with the basis set superposition error (BSSE) correction (ratio = $value_{R,R}/value_{R,S}$, gap = $\Delta E_{R,R} - \Delta E_{R,S}$).

Further evaluation was carried out using ^{1}H NMR titration experiments (Fig. 4d and e), which were consistent with the UV-vis and fluorescence titrations. Among all guests, MNA exhibited the most significant chemical shift changes upon interaction with Pyr. The chemical shift variation of MNA was plotted against the equivalents of added host (Fig. 4f). Chemical shift changes for each guest were also quantified, and the ratio between the two enantiomers of each guest was used to assess the degree of chiral recognition, which gave the same order as the UV-vis/fluorescence titration experiments (Fig. 4g). Moreover, the chemical shift changes of H_a were fitted to obtain the K_a between the host and each guest (Fig. 4h,i). The ratio of K_a values for the two enantiomers of each guest was then used to evaluate the chiral recognition ability. All host–guest combinations exhibit comparable binding strengths ($K \approx 10^3$). Among them, ^{R}MNA/^{R}Pyr displays the strongest binding affinity, with a K value of 9.6×10^3. Notably, MNA also shows the highest selectivity, with a binding ratio of $K_{R,R}/K_{R,S} = 3.25$. This behavior originates from the combined effects of molecular shape and the available aromatic surface of MNA. Local aromatic regions of MNA participate in π–π and C–H···π interactions with the host. Moreover, this conclusion is further supported by MESP analysis (Fig. S8–S15) and by the enhanced contribution of dispersion interactions revealed in the energy decomposition analysis (Table S1). For spatially matched guests, the larger aromatic surface allows more extensive dispersive interactions, leading to stronger binding, while the increased steric bulk enhances chiral selectivity. In contrast, spatial mismatch leads to inefficient aromatic overlap, increased steric repulsion, and weakened binding. Next is DHIA, which exhibits a binding ratio of 2.24. We speculate that this may be due to the host's preferential recognition of planar structures, leading to higher selectivity for DHIA compared to MBA and EBA. MBA and EBA follow, with binding ratios of 1.50 and 1.02, respectively. This trend is consistent with the order observed in both the UV-vis absorption and NMR chemical shift experiments.

Subsequently, further validation of this conclusion was achieved through computational simulations using the Gaussian 16 program at the DFT (B3LYP)/6-311G(d,p) level of theory with D3 dispersion correction, combined with basis set superposition error (BSSE). The chiral recognition ability was evaluated by comparing the binding energy gaps between the two enantiomers of each guest (Fig. 4j). The same order was obtained, further confirming the reliability of this sequence. Among the guests, MNA exhibited the highest chiral selectivity, which can likely be attributed to its larger π-conjugated system.

The importance of the aryl structure was already demonstrated in the earlier comparison between DSe and BuSe. The order DHIA > MBA > EBA may be explained by differences in steric hindrance. Smaller steric bulk facilitates deeper penetration of the guest into the chiral electronic environment of the host cavity, thereby enhancing the enantiomeric effect.

Study of chiroptical properties

Samples were prepared under solution-phase conditions for circular dichroism (CD) measurements. The chiroptical properties were studied. In the CD spectra, exciton-coupled bands were observed at around 400 nm, corresponding to the characteristic absorption peaks of Pyr (Fig. 5a). Based on the single-crystal structure of Pyr, the appearance of exciton-type signals in the CD spectrum can be attributed to the close spatial arrangement of the aromatic systems within Pyr, which leads to exciton coupling with the chiral orientation of the transition dipole moments. Upon the addition of MBA to Pyr, different chiral combinations exhibited distinct evolutions (Fig. 5b). Additionally, a new signal emerged at 430 nm. In the corresponding absorption spectra, a general decreasing trend was also observed; however, a signal inversion occurred at 350 nm, and no new peak appeared at 430 nm. The combinations with different absolute chirality exhibited more pronounced exciton-type signals, which may originate from the stronger binding activity between ^{R}Pyr and ^{S}MBA. This enhanced binding affinity brings the aromatic units into closer proximity, thereby resulting in more distinct excitonic features. These distinct patterns of supramolecular evolution suggest the presence of two different binding modes or aggregation behaviors within the supramolecular complexes.

In addition, to investigate the relationship between the supramolecular structures and chiral luminescence, samples were prepared under assembly conditions for circularly polarized luminescence (CPL) measurements (Fig. 5a). In the CPL spectra, chiral luminescence was observed at wavelengths corresponding to the emission of the assemblies. Specifically, ^{R}Pyr exhibited positive CPL, while ^{S}Pyr showed negative CPL, with a g_{lum} value of approximately ±0.015. Furthermore, CPL measurements of the host–guest assemblies revealed a general trend (Fig. S45–S48). For MBA, a slight increase in g_{lum} was observed in homochiral combinations, whereas heterochiral combinations led to a complete inversion of the CPL signal.

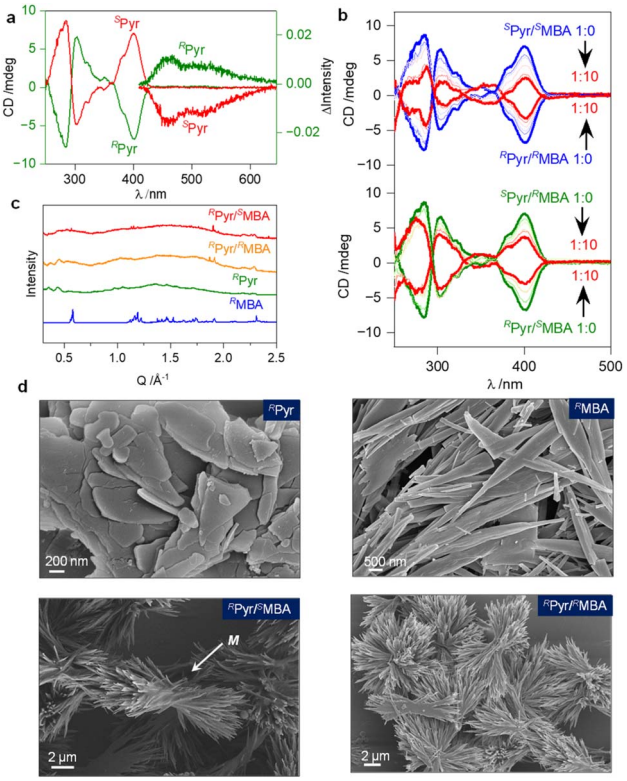

Fig. 5 (a) Circular dichroism (CD, 0.05 mM, $CHCl_3$/MCH, v/v = 1 : 39) and circularly polarized luminescence (CPL) of Pyr. CPL measurements were conducted using thin films prepared using the assembly, and the assembly was obtained by mixing Pyr and the guest at a 1 : 1 molar ratio with a concentration of 0.125 mM in a $CHCl_3$/MCH (v/v = 1 : 39) solvent system. (b) CD titration spectra for Pyr with different enantiomers of MBA. (c) The GIXS patterns and integral curves. Conditions are the same as for CPL. (d) Morphologies of different assemblies captured by scanning electron microscopy (SEM). Conditions are the same as for CPL.

Characterization of morphology and topology

To further explore the possible supramolecular arrangements, samples prepared under assembly conditions were deposited onto silicon substrates and subjected to grazing-incidence X-ray scattering (GIXS) analysis (Fig. 5c). The GIXS patterns show that both Pyr and MBA exhibit well-defined crystalline features. Comparison with the single-crystal data reveals that, under the given assembly conditions, MBA tends to adopt the β-phase. In the co-assembly phase, all pristine peaks were replaced by new peaks, implicating the formation of a new phase without inherent self-sorting. Compared to the homochiral combinations (*R*/*R* or *S*/*S*), heterochiral combinations (*R*/*S* or *S*/*R*) show stronger binding affinity, which improves the structural integrity of the complexes and enables the expression of chirality at the macroscopic scale. This observation is consistent with their different peaks, and heterochiral co-assemblies possess fewer scattering bands corresponding to the elongated one-dimensional extension with a higher aspect ratio, which facilitates the emergence of macroscopic chirality.

Samples were prepared using the same procedure as that employed for GIXS measurements, and the self-assembled nanoarchitectures were investigated by scanning electron microscopy (SEM) (Fig. 5d). Pyr exhibited a sheet-like morphology, while MBA formed fibrous structures. Upon co-assembly, the resulting structures transformed into thinner fibers that tended to aggregate into higher-order superstructures. The ^{R}Pyr/^{R}MBA co-assemblies show no expression of macroscopic chirality. In contrast, the ^{R}Pyr/^{S}MBA system forms left-handed (M-type) helical assemblies, while the ^{S}Pyr/^{R}MBA gives rise to right-handed (P-type) helices, demonstrating a consistent and reproducible correlation between the molecular chirality of the components and the helical handedness of the resulting assemblies. This helical sense originates from

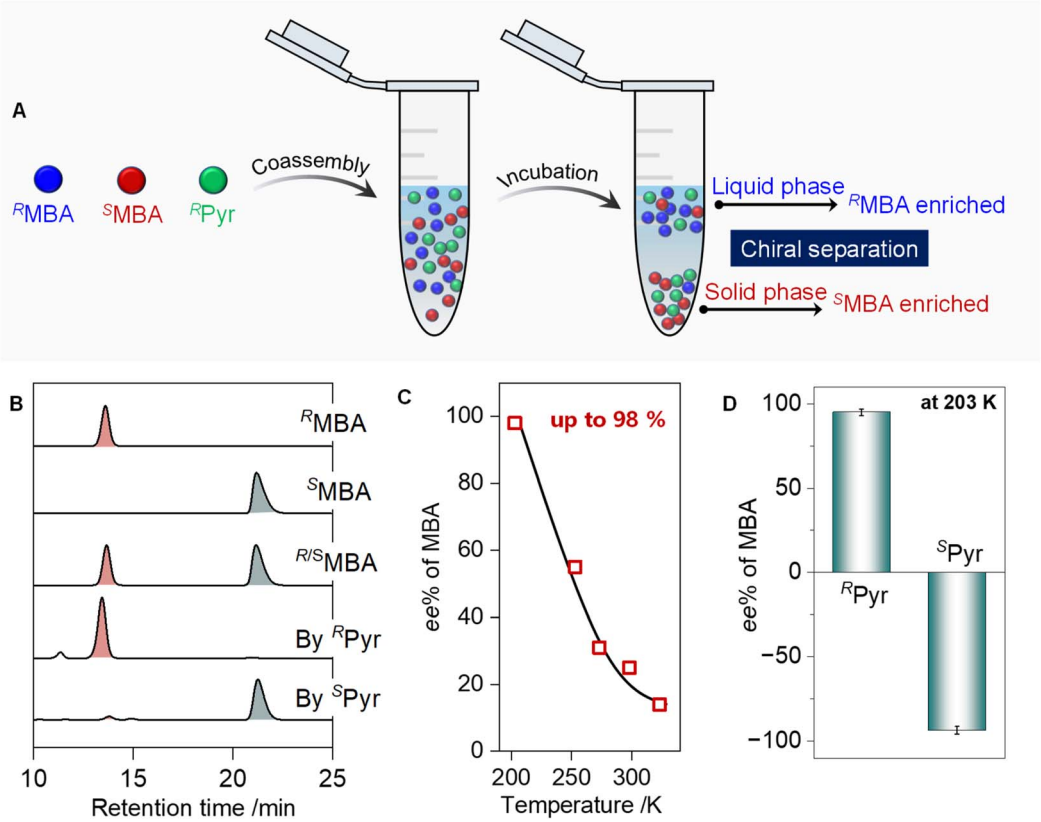

Fig. 6 (A) Schematic illustration of the chiral resolution process. (B) HPLC patterns for the MBA monomer and the resolution products. (C) Summary of enantiomeric excess values of chiral resolution results under different hosts. (D) ee% of MBA separation at different temperatures. ee% = ([*R*] − [*S*])/([*R*] + [*S*]).

a hierarchical self-assembly process, in which the intrinsic chirality of the Pyr units is retained in locally ordered subunits and subsequently biases their directional stacking, leading to a preferred sense of twist during growth. The accumulation of this biased stacking across length scales ultimately results in macroscopic helices with well-defined handedness.[47] Similar structural differences were also observed in other chiral guest systems, indicating that distinct binding modes exist in different chiral combinations (Fig. S49–S52). In light of the observed CPL trends, it is reasonable to infer that the fine fibrous structures within the assemblies enhance the chiral expression of the chromophores, thereby leading to the increased g_{lum} value observed in the ^{R}Pyr/^{R}MBA system. Moreover, the supramolecular helical structures arising from chiral evolution contribute to a secondary level of chiral expression, which accounts for the CPL signal inversion observed in the ^{R}Pyr/^{S}MBA system.

Application for enantiomer separation

An enantiomer separation strategy was developed based on the enantioselective recognition. Using the same solvent system and concentration conditions as those employed during the assembly process, environmental parameters, including temperature and aging time, were optimized. ^{R}Pyr was co-assembled with racemic MBA, followed by treatment *via* a nanoprecipitation method (Fig. 6a). The procedure is described in detail in the SI. After incubation and centrifugation, the mixture was separated into supernatant and precipitate fractions. Due to the differential binding affinities of ^{R}MBA and ^{S}MBA toward ^{R}Pyr, their distribution between the two fractions diverges accordingly. The enantiomeric excess (ee%) values of both fractions were subsequently determined by high-performance liquid chromatography (HPLC) analysis. Racemic MBA and its two enantiomers were analyzed to identify their retention times. The results showed that ^{R}MBA eluted at approximately 14 min, while ^{S}MBA eluted at around 21 min (Fig. 6b). Next, the assembled materials obtained under different temperatures were analyzed, and the corresponding ee% values are summarized in Fig. 6c. Temperature-controlled experiments revealed that lower temperatures favor chiral resolution, indicating that the binding specificity is primarily governed by kinetic factors. Among the tested conditions, the best separation was achieved after aging at 203 K for 24 hours, with an ee% up to 98%. The pronounced temperature sensitivity observed in the separation process is likely attributable to the differences in entropy changes during the recognition process. Owing to the deep chiral cavity environment of the host, the two enantiomeric guests undergo distinct recognition and binding modes, which consequently result in different entropy variations upon complex formation. To further

elucidate this behavior, the thermodynamic parameters of the systems were investigated. The calculated entropy changes for the formation of the ^{R}Pyr/^{R}MBA and ^{R}Pyr/^{S}MBA complexes were -230.074 J mol^{-1} K^{-1} and -258.613 J mol^{-1} K^{-1}, respectively. Based on the Gibbs–Helmholtz relationship, $\Delta G = \Delta H - T\Delta S$, a smaller ΔS value implies a more pronounced decrease in ΔG upon lowering the temperature. Therefore, during the competitive recognition process between ^{R}MBA and ^{S}MBA, decreasing the temperature thermodynamically favors the binding of ^{R}Pyr with ^{S}MBA. Consequently, the proportion of ^{S}MBA remaining in the liquid phase decreases, which is experimentally manifested as an increase in the ee value. Based on these findings, we developed a chiral recognition and resolution strategy mediated by ChB, addressing the current gap in the application of ChB in this field. This work expands the functional scope of ChB and paves the way for its advancement as a powerful tool in supramolecular science, chemistry, and the broader natural sciences.

Conclusions

In summary, we report a chiral recognition and separation strategy for organoselenocyanates based on ChB. To mimic the recognition behavior of biological receptors toward selenocyanate-based agents, a host molecule featuring a deep chiral cavity was rationally designed. Correspondingly, selenocyanate-based guest model compounds were synthesized based on the structural characteristics of the host. Efficient chiral recognition was successfully achieved. The recognition process was demonstrated to rely on three key noncovalent interactions: HB, π–π stacking, and ChB. Furthermore, we investigated the properties of the assembled structures and found that different chiral combinations exhibited distinct supramolecular evolution pathways across various characterization methods. Finally, leveraging the specificity of supramolecular recognition, we innovatively designed a chiral resolution strategy based on ChB, achieving a maximum ee% of 98%. This work offers an alternative perspective for the development of chiral separation methodologies. It highlights the untapped potential of ChB in chiral recognition and separation, and envisions its future as a valuable building block in the field of supramolecular chemistry.

Author contributions

Tianhao Wang: investigation, methodology, formal analysis, data curation, visualization, writing – original draft. Aiyou Hao: conceptualization, supervision, funding acquisition, project administration, writing – review & editing. Pengyao Xing: conceptualization, supervision, writing – review & editing.

Conflicts of interest

There are no conflicts to declare.

Data availability

CCDC 2469788–2469791 contain the supplementary crystallographic data for this paper.[48a–d]

The data that support the findings of this study are available from the corresponding author upon reasonable request.

Supplementary information (SI): experimental procedures, additional experimental data, synthesis and characterization. See DOI: https://doi.org/10.1039/d6sc03073d.

Acknowledgements

This work is supported by the National Natural Science Foundation of China (No. 22371170, 22571184) and the National Natural Science Foundation of Shandong Province (ZR2025QA15).

Notes and references

1 G. Wu, Y. Chen, S. Fang, L. Tong, L. Shen, C. Ge, Y. Pan, X. Shi and H. Li, *Angew. Chem., Int. Ed.*, 2021, **60**, 16594.
2 M. Hu, F. Ye, C. Du, W. Wang, W. Yu, M. Liu and Y. Zheng, *Angew. Chem., Int. Ed.*, 2022, **61**, e202115216.
3 J. Huang, Y. Liu, Y. Si, Y. Cui, X. Dong and S. Zang, *J. Am. Chem. Soc.*, 2024, **146**, 16729.
4 M. Jin, Q. Zhen, D. Xiao, G. Tao, X. Xing, P. Yu and C. Xu, *Nat. Commun.*, 2022, **13**, 3276.
5 Y. Yoshikai, T. Mizuno, S. Nemoto and H. Kusuhara, *Nat. Commun.*, 2024, **15**, 1197.
6 J. Hallin, V. Bowcut, A. Calinisan, D. M. Briere, L. Hargis, L. D. Engstrom, J. Laguer, J. Medwid, D. Vanderpool, E. Lifset, D. Trinh, N. Hoffman, X. Wang, J. D. Lawson, R. J. Gunn, C. R. Smith, N. C. Thomas, M. Martinson, A. Bergstrom, F. Sullivan, K. Bouhana, S. Winski, L. He, J. Fernandez-Banet, A. Pavlicek, J. R. Haling, L. Rahbaek, M. A. Marx, P. Olson and J. G. Christensen, *Nat. Med.*, 2022, **28**, 2171.
7 Y. Wang, X. Huang and X. Zhang, *Nat. Commun.*, 2021, **12**, 1291.
8 X. Gao and T. Ben, *Nat. Commun.*, 2025, **16**, 5210.
9 D. L. Reinhard, A. Iniutina, S. Reese, T. Shaw, C. Merten, B. List and S. M. Huber, *J. Am. Chem. Soc.*, 2025, **147**, 8107.
10 Y. C. Tse, A. Docker, I. Marques, V. Félix and P. D. Beer, *Nat. Chem.*, 2025, **17**, 373.
11 P. Peluso and B. Chankvetadze, *Chem. Rev.*, 2022, **122**, 13235.
12 S. Wang, Y. Wang, L. Huang, L. Zheng, H. Nian, Y. Zheng, H. Yao, W. Jiang, X. Wang and L. Yang, *Nat. Commun.*, 2023, **14**, 5645.
13 A. Stefani, T. Salzillo, P. R. Mussini, T. Benincori, M. Innocenti, L. Pasquali, A. C. Jones, S. Mishra and C. Fontanesi, *Adv. Funct. Mater.*, 2023, **34**, 2308948.
14 X. Chen, R. Zhu, B. Zhang, X. Zhang, A. Cheng, H. Liu, R. Gao, X. Zhang, B. Chen, S. Ye, J. Jiang and G. Zhang, *Nat. Commun.*, 2024, **15**, 3314.
15 G. Sekar, V. V. Naira and J. Zhu, *Chem. Soc. Rev.*, 2024, **53**, 586.

16 C. B. Aakeroy, D. L. Bryce, G. R. Desiraju, A. Frontera, A. C. Legon, F. Nicotra, K. Rissanen, S. Scheiner, G. Terraneo, P. Metrangolo and G. Resnati, *Pure Appl. Chem.*, 2019, **91**, 1889.
17 P. Wonner, L. Vogel, M. Düser, L. Gomes, F. Kniep, B. Mallick, D. B. Werz and S. M. Huber, *Angew. Chem., Int. Ed.*, 2017, **56**, 12009.
18 A. Docker, T. G. Johnson, H. Kuhn, Z. Zhang and M. J. Langton, *J. Am. Chem. Soc.*, 2023, **145**, 2661.
19 J. Y. C. Lim, I. Marques, A. L. Thompson, K. E. Christensen, V. V. Félix and P. D. Beer, *J. Am. Chem. Soc.*, 2017, **139**, 3122.
20 A. Docker, I. Marques, H. Kuhn, Z. Zhang, V. Félix and P. D. Beer, *J. Am. Chem. Soc.*, 2022, **144**, 14778.
21 L. M. Lee, M. Tsemperouli, A. I. Poblador-Bahamonde, S. Benz, N. Sakai, K. Sugihara and S. Matile, *J. Am. Chem. Soc.*, 2019, **141**, 810.
22 S. Benz, M. Macchione, Q. Verolet, J. Mareda, N. Sakai and S. Matile, *J. Am. Chem. Soc.*, 2016, **138**, 9093.
23 S. Benz, J. Llpez-Andarias, J. Mareda, N. Sakai and S. Matile, *Angew. Chem., Int. Ed.*, 2017, **56**, 812.
24 S. Benz, A. I. Poblador-Bahamonde, N. Low-Ders and S. Matile, *Angew. Chem., Int. Ed.*, 2018, **57**, 5408.
25 T. Murai, W. Lu, T. Kuribayashi, K. Morisaki, Y. Ueda, S. Hamada, Y. Kobayashi, T. Sasamori, N. Tokitoh, T. Kawabata and T. Furuta, *ACS Catal.*, 2021, **11**, 568.
26 X. He, Y. Fu, R. Xi, C. Zhang, K. Lan, Z. Su, F. Wang, X. Feng and X. Liu, *Angew. Chem., Int. Ed.*, 2025, **64**, e202417636.
27 J. Liu, M. Zhou, R. Deng, P. Zheng and Y. R. Chi, *Nat. Commun.*, 2022, **13**, 4793.
28 J. Fanfrlík, A. Přáda, Z. Padělková, A. Pecina, J. Macháček, M. Lepšík, J. Holub, A. Růžička, D. Hnyk and P. Hobza, *Angew. Chem., Int. Ed.*, 2014, **53**, 10139.
29 S. Kolb, G. A. Oliver and D. B. Werz, *Angew. Chem., Int. Ed.*, 2020, **59**, 22306.
30 T. Inoue, M. Ota, Y. Amijima, H. Takahashi, S. Hamada, S. Nakamura, Y. Kobayashi, T. Sasamori and T. Furuta, *Chem.–Eur. J.*, 2023, **29**, e202302139.
31 T. Fellowes, E. Lee, J. Tran, R. Xu, A. Barber, S. C. Brydon, J. K. Clegg and J. M. White, *Cryst. Growth Des.*, 2023, **23**, 7179.
32 Y. Xu, V. Kumar, M. J. Z. Bradshaw and D. L. Bryce, *Cryst. Growth Des.*, 2020, **20**, 7910.
33 B. J. Eckstein, L. C. Brown, B. C. Noll, M. P. Moghadasnia, G. J. Balaich and C. M. McGuirk, *J. Am. Chem. Soc.*, 2021, **143**, 20207.
34 J. Y. C. Lim, I. Marques, V. Félix and P. D. Beer, *Chem. Commun.*, 2018, **54**, 10851.
35 P. Pelusoa, C. Gatti, A. Dessì, R. Dallocchioa, R. Weiss, E. Aubert, P. Pale, S. Cossu and V. Mamane, *J. Chromatogr. A*, 2018, **1567**, 119.
36 W. Hou and H. Xu, *J. Med. Chem.*, 2022, **65**, 4436.
37 C. Morán-Serradilla, D. Plano, C. Sanmartín and A. K. Sharma, *J. Med. Chem.*, 2024, **67**, 7759.
38 S. Ramos-Inza, A. C. Ruberte, C. Sanmartín, A. K. Sharma and D. Plano, *J. Med. Chem.*, 2021, **64**, 16380.
39 X. He, M. Zhong, S. Li, X. Li, Y. Li, Z. Li, Y. Gao, F. Ding, D. Wen, Y. Lei and Y. Zhang, *Eur. J. Med. Chem.*, 2020, **208**, 112864.
40 T. Wang, Z. Zhang, A. Hao and P. Xing, *Chem. Sci.*, 2025, **16**, 3498.
41 Z. Wang, A. Hao and P. Xing, *Small*, 2024, **20**, 2407149.
42 M. Cao, L. Wang, H. Gao, H. Jiang and H. Song, *New J. Chem.*, 2023, **47**, 1797.
43 S. L. W. McWhinnie, A. B. Brooks and I. Abrahams, *Acta Crystallogr. Sect. C Cryst. Struct. Commun.*, 1998, **C54**, 126.
44 A. Lari, R. Gleiter and F. Rominger, *Eur. J. Org Chem.*, 2009, **14**, 2267.
45 H. Huynh, O. Jeannin and M. Fourmigué, *Chem. Commun.*, 2017, **53**, 8467.
46 V. Kumar, M. Triglav, V. M. Morin and D. L. Bryce, *ACS Org. Inorg. Au*, 2022, **2**, 252.
47 Z. Wang, Y. Gai, A. Hao and P. Xing, *Angew. Chem., Int. Ed.*, 2025, **64**, e202501832.
48 (*a*) CCDC 2469788: Experimental Crystal Structure Determination, 2026, DOI: 10.5517/ccdc.csd.cc2nx0l6; (*b*) CCDC 2469789: Experimental Crystal Structure Determination, 2026, DOI: 10.5517/ccdc.csd.cc2nx0m7; (*c*) CCDC 2469790: Experimental Crystal Structure Determination, 2026, DOI: 10.5517/ccdc.csd.cc2nx0n8; (*d*) CCDC 2469791: Experimental Crystal Structure Determination, 2026, DOI: 10.5517/ccdc.csd.cc2nx0p9.